Continental Shelf Research 33 (2012) 1–13

Contents lists available at SciVerse ScienceDirect

Continental Shelf Research

journal homepage: www.elsevier.com/locate/csr

Review papers

Surface current variability and wind influence in the northeastern Adriatic Sea as observed from high-frequency (HF) radar measurements

Simone Cosoli [a,*], Miroslav Gačić [a], Andrea Mazzoldi [b]

[a] Istituto Nazionale di Oceanografia e Geofisica Sperimentale, Borgo Grotta Gigante 42/c, 34010 Sgonico, Trieste, Italy
[b] Istituto di Scienze Marine, Consiglio Nazionale delle Ricerche, Sezione di Venezia, Italy

ARTICLE INFO

Article history:
Received 3 March 2011
Received in revised form
11 November 2011
Accepted 15 November 2011
Available online 26 November 2011

Keywords:
Adiatic Sea
High-frequency radars
Surface circulation
Tides
Wind-driven currents

ABSTRACT

A network of HF radars operated in the northeastern Adriatic Sea in the period September 2007 to August 2008. Surface currents were collected with the purpose of studying the temporal and spatial modes of surface circulation in the area. Their dependence on local wind forcing was investigated using wind records from coastal stations and the mesoscale meteorological model ALADIN/HR. EOF decomposition, spectral and tidal analyses, and time-lagged correlation extracted the dominant features in the area and their time scales. The time-averaged flow presented a cyclonic circulation pattern with relatively weak currents and standard deviations comparable to average values. Three dominant current patterns were extracted by the EOF analysis, which accounted for about 70% of total variance. In the region, wind was the major source of current variability over a wide portion of frequencies, whereas tidal forcing was weak and limited to the semidiurnal and diurnal frequencies, representing 10%–20% of the total variance. The response to wind forcing was immediate with veering angles consistent with Ekman dynamics in the majority of the area. Coherence analyses revealed strong correlation within the sub-tidal and diurnal bands, the latter related to diurnal sea-breezes variability. The seasonal variability of the inertial motions was also observed in the area.

Contents

1. Introduction

The Adriatic Sea is a semi-enclosed marginal sea in the northeastern Mediterranean area, elongated in a NW–SE direction and confined by the Italian peninsula to the west and the Balkans to

* Corresponding author. Tel.: +39 0402140371; fax: +39 0402140266.
E-mail address: scosoli@ogs.trieste.it (S. Cosoli).

0278-4343/$ - see front matter © 2011 Elsevier Ltd. All rights reserved.
doi:10.1016/j.csr.2011.11.008

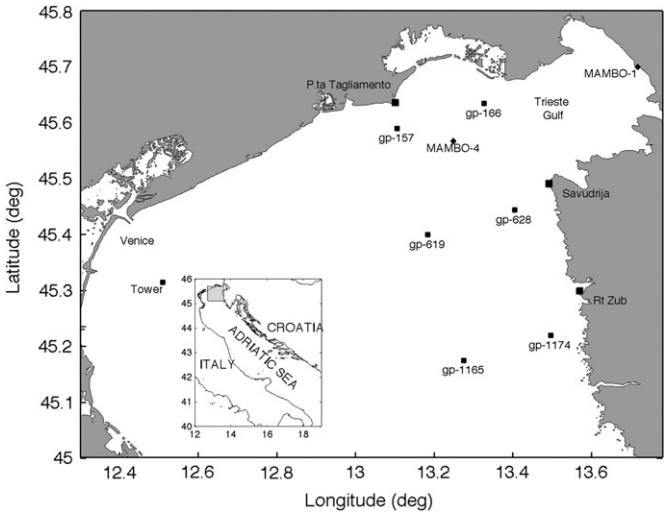

Fig. 1. The study area, located in the northeastern corner of the Adriatic Sea, with the locations of the radard stations used in this study (Rt Zub, Savudrija to the East, and P.ta Tagliamento to the North) and the locations of the MAMBO buoys. The locations of six grid points in the radar domain are also shown. These points were used to describe the surface current variability at selected locations.

the east (Fig. 1). Its circulation is usually described as a basin-wide cyclonic structure, since it is composed by a combination of northwestwards inflow on the eastern side (Eastern Adriatic Current, EAC), and a southeastward flow (Western Adriatic Current, WAC) on the western side of the basin (Orlić et al., 1992) This WAC–EAC current system is primarily sustained by thermohaline forces and secondarily by strong wind pulses (Hopkins et al., 1996; Book et al., 2007). Cyclonic recirculation cells occurring at a sub-basin level (Poulain, 2001) enrich the basin-wide counter-clockwise circulation scheme.

In recent years, the Adriatic Sea circulation has been focus of a number of studies devoted to its dominant features and their temporal and spatial scales (see, for instance, Cushman-Roisin et al., 2001). Several oceanographic programs, focused on the northern sub-basin, made extensive use of field observations (CTD probes, current meter moorings at selected locations; ship-mounted ADCP's), circulation models, and a variety of platforms (HF radars; drifters). Amongst them: ELNA–Eutrophic Limits of the Northern Adriatic (Hopkins et al., 1996); ACE–Adriatic Circulation Experiment (Book et al., 2007); DOLCEVITA (Dynamics of Localized Currents and Eddy Variability in the Adriatic).

The dominant wind regime, or the freshwater input from the local rivers, may introduce intensifications or departures from the basic circulation scheme at a local scale. Inversions of the dominant flow direction, as well as intensifications of the WAC, have been documented for instance offshore Venice and Ancona as a response to either southerly winds or intense northeasterly winds (Kovačević et al., 2000; Kovačević et al., 2004; Book et al., 2007). Strong currents in the opposite direction of the EAC appear also in the coastal strip along the Istrian peninsula, in response to anomalous winter-time heat gain in addition to significant transversal transport of fresh water from the Po river. This latter current, known as the Istrian Coastal Countercurrent (ICCC), reflects changes in the current regime of the Istrian coastal belt extending some 20 Nm offshore, and is confined to the upper layer (20 m depth) of the water column (Supić et al., 2000a, 2000b, 2003).

Despite the abundance of oceanographic programmes that investigated the hydrography of the area, there appears to exist a lack of direct information on current measurements, with the exception of localized current meter moorings (for instance, Book et al., 2007). With respect to pointwise current measurements, HF radars provide an unprecedented coverage in space and time of sea-surface currents in the area since they ensure a synoptical view of the current field at distances of tens to hundreds kilometers from shore. This is a particularly important aspect since the northern Adriatic Sea is heavily impacted by shipping activities, which might compromise fishing activities and determine losses of touristic revenue in the area.

In spite of the fact that HF radars only provide a view of the ocean circulation limited to a surface skin layer, this technology is widely used in oceanographic studies. Observing networks that make extensive use of HF radars exist along the US coasts and are spreading across Europe. HF radars in the Adriatic Sea have been previously deployed offshore Ancona (Kovačević et al., 2000; Budillon et al., 2002), to the South of the Po river (Chavanne et al., 2007), and offshore the Venice Lagoon area, revealing previously unreported circulation features (Kovačević et al., 2004; Book et al., 2005; Gačić et al. 2009). Qualitative and quantitative validation studies evidenced the reliability of surface HF radar current measurements over a variety of deployment scenarios (Chapman and Graber, 1997; Kohut and Glenn, 2003; Emery et al., 2004). Similarly, radar capabilities have been demonstrated in the northern Adriatic Sea, a shallow-water area in which typical currents are weak and comparable with the radar uncertainty levels (Mazzoldi et al., 1998; Cosoli et al., 2005, 2008, 2010).

This study focuses on surface current observations in the northeastern corner of the Adriatic Sea, along the coast of Italy and the Istrian peninsula adjacent to the Gulf of Trieste. It explores the structures, the modes of variability and the dominant time scales of surface circulation as observed using high-frequency (HF) radars for the period 2007–2008. Attention is given in particular to the role of wind, since surface current patterns are, for the most part, under a major influence of local wind forcing, especially when wind speed exceeds a certain threshold (Ursella et al., 2006; Gačić et al., 2009).

2. Materials and methods

This work is primarily based on surface current measurements collected in the northeasternmost part of the Adriatic Sea (Fig. 1) for the period September 2007–August 2008. Current maps were collected with high-frequency (HF) radars as part of the Northern Adriatic Sea Current Monitoring (NASCUM) INTERREG initiative between Italy and Croatia, conducted under the sponsorship of the European Union. In this paper wind fields from the high-resolution meteorological ALADIN/HR model (Ivatek-Šahdan and Tudor, 2004) are used, as well as data from two coastal stations along the Italian coast, in order to provide an insight on the typical time scales and modes of variability of the surface currents and their response to wind forcing.

2.1. HF radar data

HF radars measure surface currents by determining the Doppler shift of an electromagnetic wave reflected from surface gravity waves at half the wavelength of the transmitted wave (Paduan and Graber, 1997). Since a single radar station measures the radial component of the surface current vector approaching to or receding from the receiver, two or more HF radar stations are required to resolve the two-dimensional flow field in an area of common signal overlap. The HF radars used in this study (SeaSonde HF radars) were installed along the Istrian and the Italian coast starting from July 2007. Two stations, named PZUB (Rt Zub) and SVDR (Savudrija) became operative between July and

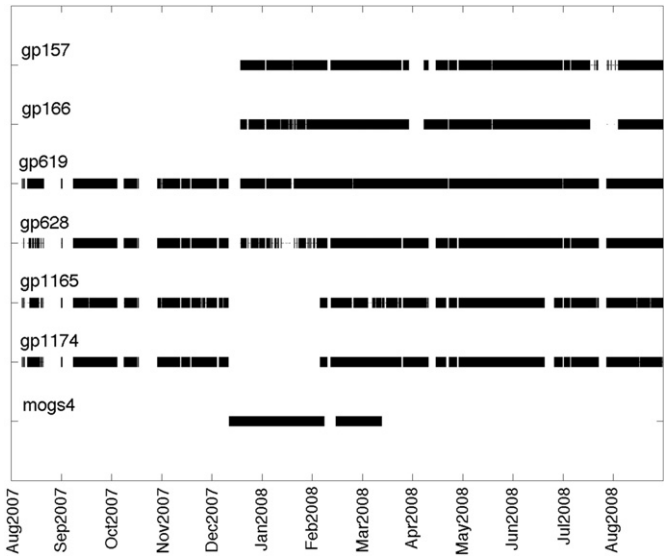

Fig. 2. Diagram of data availability of sea-surface currents at six grid points in the radar domain. The data availability for the moored current meter used for the error analysis is also shown. Their locations are illustrated in Fig. 1.

Table 1
Start, end period, and number of hourly valid observations for each grid point included in the analyses (see Fig. 1 for their location within the radar domain). All times are UTC.

Grid point	Start time	End time	No. of valid observations
157	Dec.18, 2007, 1000	Aug. 31, 2008, 2300	5337
166	Dec.18, 2007, 1000	Aug. 31, 2008, 2300	5320
619	Sept. 1, 2007, 0000	Aug. 31, 2008, 2300	7749
628	Sept. 1, 2007, 0000	Aug. 31, 2008, 2300	7121
1165	Sept. 1, 2007, 0000	Aug. 31, 2008, 2300	5857
1174	Sept. 1, 2007, 0000	Aug. 31, 2008, 2200	6219

August 2007. A third HF radar, named BBIN (Bibione – Punta Tagliamento) was added to the existing network in December 2007 (Fig. 2; see also Table 1). HF radars operated in the 25 MHz frequency band at a 100 kHz bandwidth (1.5 km resolution in range) and 5° resolution in angle, and provided radial current maps at 1 h temporal resolution using the ideal antenna patterns with their phases corrected after the pattern measurements. The choice of the ideal patterns was dictated by a severe distortion in the measured pattern at Savudrija site, and in light of the previous experiences offshore the Venice Lagoon (Cosoli et al., 2010).

Hourly surface current vectors were derived following an unweighted least-squares approach that mapped the radial velocities onto a regular grid with 2 km × 2 km horizontal resolution (Gurgel, 1994). The averaging circle was set to 5 km. Methods similar to those proposed by Barth et al. (2010), in which radial velocities are weighted by their signal-to-noise ratios, were also implemented (Cosoli and Bolzon, 2009) and are being discussed in a dedicated paper (Cosoli S., Mazzoldi A., Bolzon G., Near-real time and offline signal-to-noise ratio quality control procedure for SeaSonde HF radars, in preparation).

The mapping procedure excluded grid points having large geometrical dilution of precision (GDOP) due to poor intersecting beam geometry (Chapman and Graber, 1997). The mapping procedure also excluded from the computation those grid points in which each radar site contributed with less than two radial velocities. Cut-off filters were applied on both the radial and the total vectors velocities (1.5 m s^{-1} and 1 m s^{-1}, respectively). Current vectors at each grid point were checked for spikes prior to further analyses, as described in Kovačević et al. (2004). Under the PZUB–SVDR two-sites configuration, the grid had a circular shape with approximately 20 km radius, which ensured good coverage in the region offshore the Istrian peninsula. The geometrical constraints in the intersection beam geometry (θ) were set $30^\circ < \theta < 150^\circ$. When the third HF radar system (BBIN) was added to the existing network (December 2007) the grid coverage increased to approximately 30 km × 20 km, and relaxed the geometrical constraints in the area of overlap of the three radars.

2.2. Wind and moored current meter data

The Croatian Meteorologic and Hydrological Service (DHMZ) provided high-resolution ALADIN/HR wind fields over the Adriatic Sea at 3-hours interval over a 2 km × 2 km grid for the period in which radars operated (September 2007–August 2008). Measured winds from the "MAMBO-1" meteorological buoy located inside the Trieste Gulf (45°41.95′N–13°42.99′E), and from the oceanographic tower offshore Venice (45°18.88′N–12°30.49′E) were also available (Fig. 1). Wind stress time series were derived from the horizontal components of wind velocity at the standard 10-m reference height following Large and Pond's (1981) formulation for both observed and model data.

Moored current records were available from a downward-looking 1000 kHz Aquadopp Profiler (AQP) on the "MAMBO-4" oceanographic buoy outside the Trieste Gulf (43°33.95′N to 13°14.86′E), at approximately the midpoint of the baseline connecting SVDR and BBIN radars (Fig. 1). Moored data were made available thanks to the Civil Protection, Friuli Venezia-Giulia (Italy) region. The current meter provided measurement with a temporal resolution of 5 min and a vertical resolution of 1 m. Quality-controlled data were hourly averaged around the cardinal hour so to match as close as possible the radar processing scheme. The level closest to surface was set at a nominal depth of 1.55 m.

2.3. Analysis methods

Surface currents were analyzed in time and frequency domain in order to extract their dominant spatial features and corresponding time scales. Grid points were included in the analyses if they satisfied a mimimum data return of 50%. When needed, data gaps at each grid point were filled in time using linear interpolation or in space, by averaging observations from the surrounding locations.

Tidal analyses were performed on the non-interpolated, complex-valued current vectors using the t_tide Matlab package (Pawlovitz et al., 2002). Tidal constituents with signal-to-noise ratio (snr) greater than, or equal to 1, were used to obtain tidal currents at each grid point. The record length allowed for the extraction of the dominant tidal constituents at semidiurnal (M_2, S_2) and diurnal (K_1) frequencies. Non-tidal currents were derived subtracting the synthetic time series from the hourly observations. Subtidal currents were derived from the detided currents using a 4th order Butterworth filter with a cutoff frequency $\omega = 0.0303$ cph ($T = 33$ h). Least-squares harmonic analyses were also performed on wind data at the buoy and at selected locations within the radar domain.

A least-squares fit approach was used to extract a diurnal-period component ($T = 24$ h) from current and wind records. This approach rather than least-squares tidal fit was chosen since the record length did not allow for an adequate frequency resolution within the diurnal frequency band. Good resolution is indeed needed to separate the "true" tidal constituent from non-tidal wind-driven diurnal components. Similarly, inertial oscillations were extracted from non-tidal currents by least-squares fitting a

discrete number of frequencies centered on the local inertial period (17-h at the local latitudes). Similarly to the extraction of the diurnal band signal, the least-squares fit approach was preferred to a more conventional bandpass filter in order to attenuate losses of spectral energy at the tails of the inertial and diurnal peaks introduced by the filtering process.

Additional analyses and computations involved rotary spectral analyses (Gonella, 1972), vector cross-correlation (Kundu, 1976), Empirical Orthogonal Function (EOF) analyses (Kaihatu et al., 1998; Marmorino et al., 1999), and vorticity and divergence computations. Rotary spectral analyses and EOF decomposition were performed on the complex-valued surface currents and winds. Power spectral densities, coherences and phases were obtained using 512-h data segments with 50% overlap and a Hanning window. Confidence levels for spectral densities were derived assuming a χ^2 distribution for variance, while the 95% confidence limits on coherence estimates were derived as described in Emery and Thomson (2004). Confidence levels for the eigenvalues in the EOF analysis were derived by estimating the equivalent degrees of freedom of surface currents from the autocorrelation function of the complex-valued time series at each grid point. For vector correlation analyses, confidence levels on correlation magnitudes and veering angles were derived from the percentiles of the sampling distributions of the statistics obtained following a bootstrap approach (Breaker et al., 1994; Efron and Tibshirani, 1986) in which the original horizontal components of surface currents (u,v) and wind stress (τ_x,τ_y) were resampled to produce new currents and wind stress time series. This procedure was repeated $n=1000$ times and magnitudes and veering angles were estimated for each resampled pair to generate a distribution of currents-to-wind correlation. Then, the 95% confidence intervals for vector correlation were obtained from the 2.5% and 97.5% percentiles of the bootstrap distribution.

Time series of current vorticity ($\zeta_{HF}=\partial v/\partial x-\partial u/\partial y$) and divergence ($\partial u/\partial x+\partial v/\partial y$) were computed at each grid point in the radar domain that satisfied the minimum data return threshold, passed the quality control procedures and had low GDOP values. Wind stress curl ($\zeta_{\tau w}=\partial\tau_y/\partial x-\partial\tau_x/\partial y$) was also computed on the wind field grid. For both surface currents and wind stress, the spatial gradients required for the computations were calculated by locally least-square fitting a velocity plane to each grid point using current measurements from nearby locations (Sanderson, 1995).

3. Results

3.1. Error analysis

In order to assess the reliability of radar surface currents, an error analysis is first performed on the radial velocities from individual radar sites. The baseline analysis approach is adopted (Atwater and Heron, 2010; Paduan et al., 2006), along with comparisons with a moored current meter deployed in the radar coverage (Cosoli et al., 2010; Emery et al., 2004), aimed at determining measurement errors, biases and bearing offsets on radial velocity measurements.

Comparisons with moored current meters provide an estimate of the measurement errors and biases that include the contribution of the "geophysical noise", i.e., intrinsic variability that can not be resolved given the different sampling scales. Baseline analyses provide an insight on the radar performances at midpoint of the line connecting two radars, where radial speeds are expected to have the same magnitude but opposite sign, with the advantage that comparisons are carried out on similar patches of ocean. The extension of the current meter-to-radar and the radar-to-radar radial velocities with measurements at angular sectors with fixed distance from the radar provide estimates of bearing offsets. The comparison metrics involves the calculation of correlation coefficients and rms differences, and slopes and intercepts of the regression line between the radial velocity components at the mid-point of the baseline. Moored currents are projected onto the radar-look direction prior to any comparison.

There are two baselines in the HF radar network (PZUB–BBIN; BBIN–SVDR), which increase to five (PZUB-mogs4; SVDR-mogs4; BBIN-mogs4) when the mogs4 MAMBO buoy is included in the analysis. The PZUB–SVDR baseline presents many points on land, and needs to be studied separately.

In the site-to-site baseline comparisons (Table 2), angular shift are present in the range 10–20°, but only in the case of SVDR–BBIN (SVDR side; angular offset 20°) the bearing offset is statistically significant. Correlation and rms differences are found in the range $r=[0.53; 0.65]$ and [7.5 cm s^{-1}; 9.9 cm s^{-1}], values that are common to many locations elsewhere (see for instance, Emery et al., 2004) and consistent with previous studies in the area (Cosoli et al., 2010). As for the PZUB–SVDR baseline, the analysis method proposed in Atwater and Heron (2010) shows correlation slightly exceeding $r=0.4$ between radial velocities along the perpendicular to the baseline center for distances up to 15 km (rms differences in the range 8 cm s^{-1} to 12 cm s^{-1}), and lower correlation with higher rms differences at further ranges.

The comparison with the moored current meter gives correlation in the range $r=[0.51; 0.57]$, with rms differences in the range [7 cm s^{-1}; 10 cm s^{-1}] for PZUB and BBIN. No significant angular offsets are detected for these radars, since confidence levels for the regression line parameters at the two angles largely overlap. As for SVDR radar, the comparison metrics of the radial velocities at the antenna bearing in the direction of the buoy is low ($r=0.27$; rms differences 11.79 cm s^{-1}). The angular sector that best matches the current meter records is found 30° apart from the radar-look angle ($r=0.58$; rms differences 8.42 cm s^{-1}).

3.2. Dominant features of the flow

The time-averaged circulation in the northeastern Adriatic Sea (Fig. 3) is characterized by a cyclonic circulation pattern with a northwards flow to the East along the Istrian peninsula and a jet-like southwestwards return flow to the North along the Italian coast. Magnitudes of the time-averaged flow are weak, since they barely exceed 10 cm s^{-1} to the North and being almost zero-valued offshore Rt Zub in the southwestern area. Currents exhibit a significant variability in time since velocity components have their standard deviations comparable to, or one order of magnitude larger than the mean values. The corresponding standard deviation ellipses are almost circular, with the exception of a few locations along the Italian coast to the North where they show a slightly more elongated shape.

The cyclonic circulation scheme is persistent since it is reproduced on a monthly basis with only minor deviations from the basic scheme. In general, the jet-like structure to the North is intensified during winter months and in early spring period when wind forcing is more intense. The most significant deviations occur in fall 2007 (November and December), and summer 2008 (June), when a cyclonic structure appears offshore Rt Zub and dominates the southernmost portion of the radar coverage. Westwards components appear occasionally in the coastal strip to the south of Savudrija, with the effect of deviating (January and February 2008) or interrupting the along-shore flow component in the area. This is particularly evident during winter months (December 2007 through February 2008), and it is also present in June 2008.

Current variances changes both in space and in time. In general, variances are higher along the Italian coast to the north and towards the center of the basin (200 cm^2 s^{-2}, and 300 cm^2 s^{-2},

Table 2
Summary of comparison statistics for the baseline and the moored current meter pairs. The HF site name and mooring name abbreviations are described in the text. Units for rms and intercept values are cm s^{-1}. Analyses are carried out for the time interval January 1st, 2008 through March 29th, 2008, for the radar-to-radar baseline comparison, and January 1st, 2008 through March 13th, 2008, for the radar-to-current meter comparison. 95% confidence levels (CL) for slopes and intercepts are also provided.

	θ	ρ	Δ_{vrms}	slope	95% CL	intercept	95% CL
SVDR-BBIN baseline							
Midpoint statistics – SVDR side	151	0.55	9.52	0.7064	0.6633; 0.7485	−3.6	−4.1844; −3.0185
Maximum correlation statistics – SVDR side	131	0.65	7.56	0.8745	0.8201; 0.9290	−4.59	−5.1861; −4.0038
Midpoint statistics – BBIN side	330	0.55	9.52	0.6939	0.6525; 0.7352	−0.9675	−1.5791; −0.3559
Maximum correlation statistics – BBIN side	315	0.59	8.70	0.7593	0.6603; 0.8581	−5.9381	−7.373; −4.500
PZUB-BBIN baseline							
Midpoint statistics – PZUB side	135	0.53	9.92	0.6997	0.6526; 0.7478	−4.883	−5.3794; −4.3972
Maximum correlation statistics – PZUB side	120	0.61	8.20	0.8072	0.7644; 0.8500	−3.29	−3.7435; −2.8434
Midpoint statistics – BBIN side	315	0.53	9.92	0.5801	0.5402; 0.6200	1.57	1.0686; 2.0804
Maximum correlation statistics – BBIN side	305	0.55	9.37	0.6041	0.5640; 0.6448	1.2489	−7.373;4.500
PZUB-MAMBO4 buoy							
Radar-look direction statistics	130	0.52	7.4	0.5866	0.5469; 0.6264	−2.3396	−2.6857; −1.9935
Maximum correlation statistics	120	0.57	7.07	0.6149	0.5765; 0.6532	−1.3912	−1.7565; −1.0261
SVDR-MAMBO4 buoy							
Radar-look direction statistics	156	0.27	11.79	0.2091	0.1750; 0.2432	0.5897	−1.0209; −0.1585
Maximum correlation statistics	126	0.58	8.42	0.4659	0.4360; 0.4957	1.0535	0.7296; 1.3774
BBIN-MAMBO4 buoy							
Radar-look direction statistics	326	0.51	10.8	0.3946	0.3660; 0.4225	−0.6951	−1.1084; −0.2820
Maximum correlation statistics	315	0.53	10.3	0.4180	0.3870; 0.4487	−0.5828	−1.0120; −0.1537

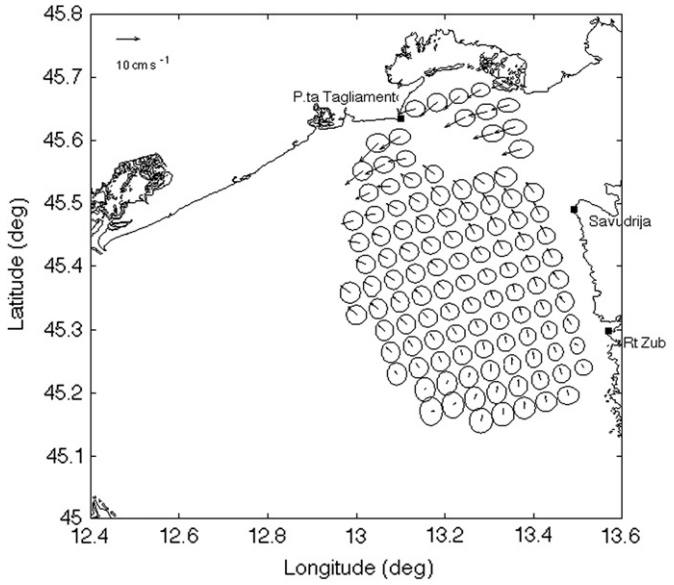

Fig. 3. Timeaveraged flow pattern for the period September 2007–August 2008, and correponding standard deviation ellipses. Current vectors are subsampled to 4 km × 4 km resolution for clarity.

corresponding to 14 cm s^{-1} and 17 cm s^{-1} rms values), with persistent minima along the Istrian coast, presenting however a seasonal cycle with the highest values during the warm seasons, that involve the entire radar domain and in particular the offshore area.

The time-averaged flow has weak and positive relative vorticity, with typical values one to two orders of magnitude smaller than the planetary vorticity *f*. Relative vorticity increases northwards in the direction of the Italian coastline and reach its maximum amplitude a few kilometers offshore Bibione–P.ta Tagliamento in the shallowest area ($\zeta_{HF} = 1.3 \times 10^{-5}$ Hz; Fig. 4a). Isolated patches with relatively strong positive vorticity associated with an increased flow curvature are found offshore Rt Zub and towards the center of the basin. Weakly negative vorticity is found on a narrow coastal strip to the SW Cape Savudrija. With the exception of a few isolated spots with

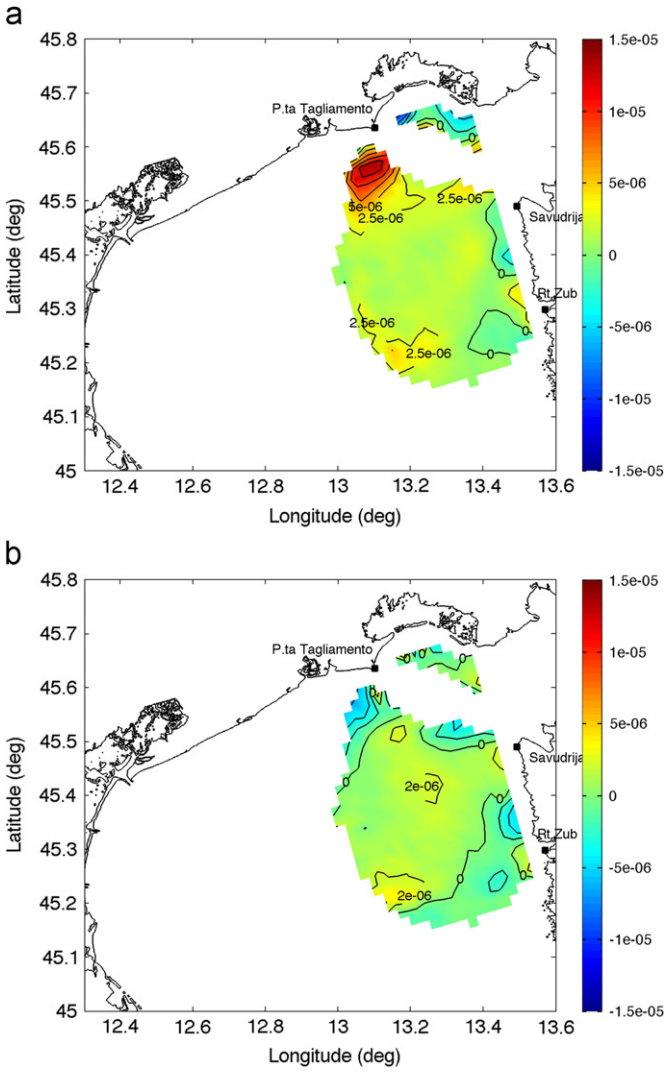

Fig. 4. Relative vorticity (upper panel) and divergence (lower panel) for the time averaged flow patterns. Units are s^{-1} (Hz).

negative divergence offshore and along the coast northwest of Rt Zub, and offshore Cape Savudrija, divergence (Fig. 4b) is positive and follows the increase and decrease of flow vorticity in the interior of the radar coverage.

3.3. Spectral properties of currents

In terms of their spectral properties, surface currents within the radar domain present common patterns and some peculiar characteristics. Common to all rotary spectra is the presence of energetic low-frequency sub-tidal ($\omega < 0.03$ cph) signals and the lack of high-frequency motions ($\omega > 0.10$ cph), along with energetic peaks at the diurnal, semidiurnal and inertial frequencies (Fig. 5). In general, energy levels in the subtidal and diurnal frequency bands are equally partitioned between the cyclonic and anticyclonic components. Locally, small differences in variance distribution are observed in the low frequency band, with counterclockwise motions being slightly more energetic than the counter-rotating components, but they are anyhow far from being statistically significant.

The most significant differences in variance distribution are found in the anticyclonic spectrum for the frequency band spanning the diurnal to inertial components. Diurnal peaks are more pronounced close to the Italian coast to the north, with amplitudes decreasing southwards in direction of Rt Zub station in the Istrian coast. On the other hand, the inertial oscillations increase their variances in direction of the center of the basin (Fig. 5, panels (b)–(e)).

Spectral properties also change in time. As evidenced for grid point gp-619 (Fig. 6a), the diurnal and the inertial frequencies show variance maxima in spring and summer, while the low-frequency

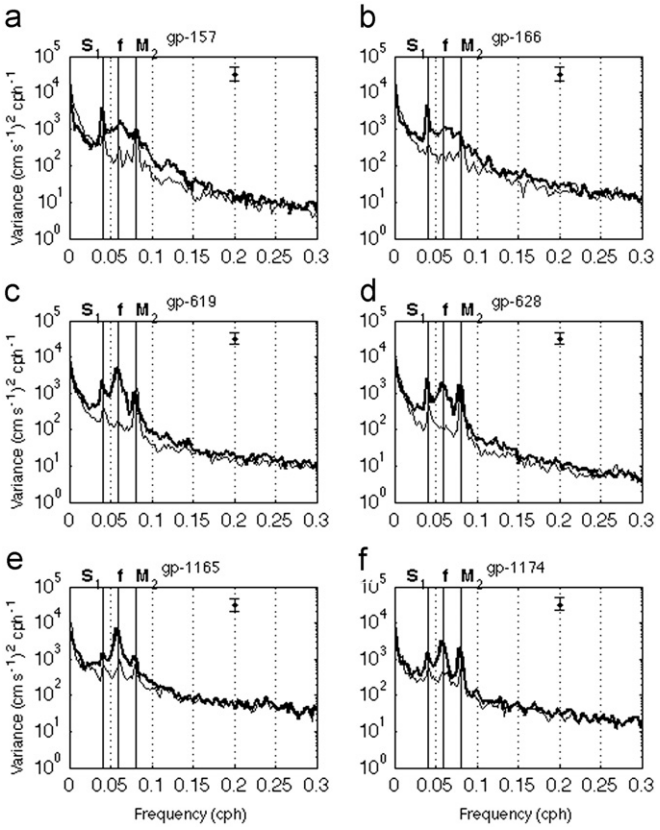

Fig. 5. Rotary spectra for surface currents at 6 locations in the radar coverage. Thin lines refer to the cyclonic motions, bold lines represent anticyclonic oscillations. Units are $cm^2\ s^{-2}$ for variance, cph for frequencies. Vertical lines denote the dominant semidiurnal (M_2), inertial (f) and diurnal (K_1) frequencies.

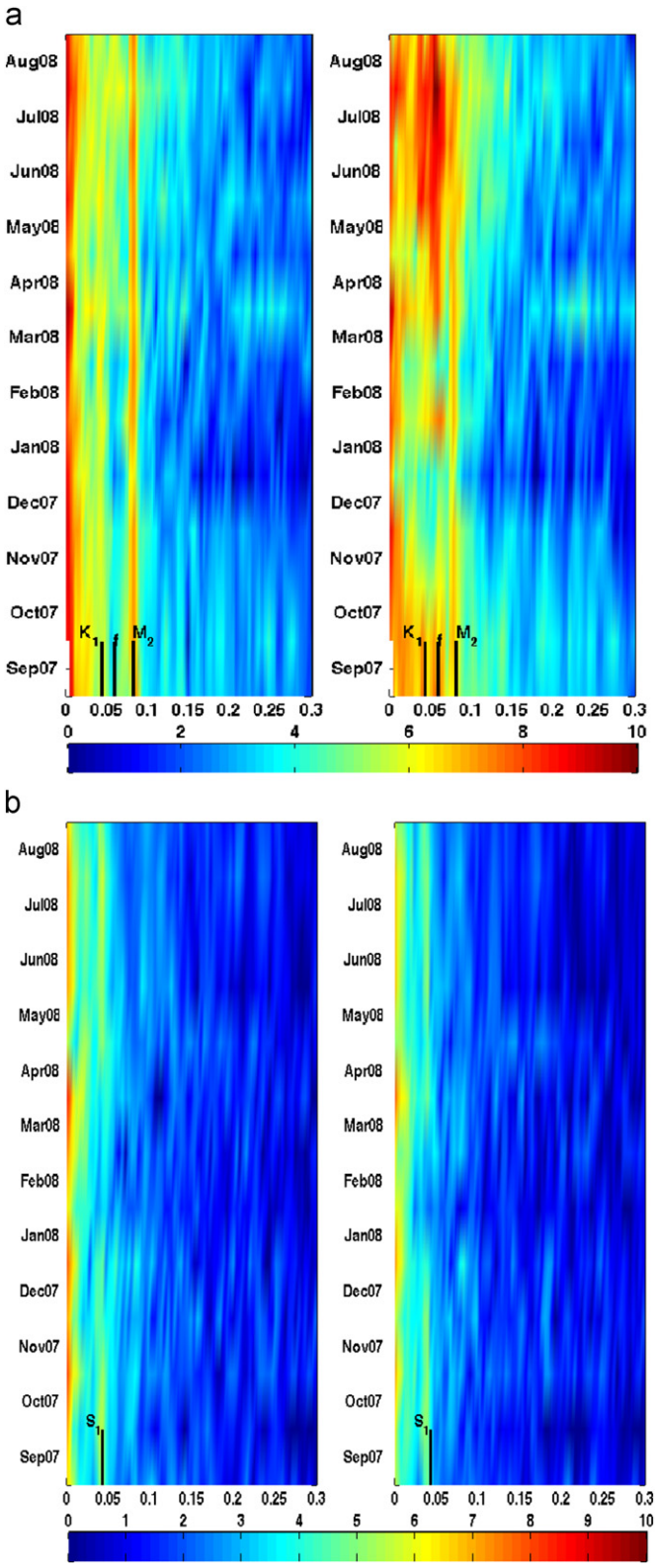

Fig. 6. (a) Monthly rotary spectra for surface currents at grid point 619, the point with the longest data set (see Fig. 1 for its location within the radar domain). Left and right panels refer to the for cyclonic and anti-cyclonic components of the spectrum, respectively. Units are $(cm\ s^{-1})^2$ for variances, *cph* for frequencies. The frequencies of the dominant harmonics (semidiurnal, inertial, and diurnal components) are shown. (b) Monthly rotary spectrum for wind stress data at the MAMBO buoy. Left and right panels present respectively variance distribution for cyclonic and anti-cyclonic components. The line shows the frequency of the diurnal component (period 24 hours) coincident with the S_1 harmonic. Units are $(N\ m^{-2})^2$ for variances, *cph* for frequencies.

band increases its variance levels in winter and spring months (December 2007, January 2008, April 2008). Similarly to surface currents, wind spectra show a decreasing variance in the diurnal bandwith as distance from the Italian coast increases, along with a seasonal increase with maxima during spring and summer (April 2008–August 2008; Fig. 6b).

3.4. Diurnal and semidiurnal frequency band: tides

Of the seven dominant tidal harmonics usually considered in the tidal analyses of the Adriatic Sea sea-surface levels and currents (O_1, P_1, K_1 for the diurnal band; N_2, M_2, S_2, K_2 for the semidiurnal band), only two diurnal (P_1, K_1) and two semidiurnal (M_2, S_2) constituents contribute significantly to tidal variances (Table 3).

Tidal forcing explains 5% to 35% of current variance in the area, with variances of the synthesized tidal currents in the range 18–70 $cm^2\ s^{-2}$ (rms values 4.3–8.4 $cm\ s^{-1}$). Tidal variance distribution within the radar domain presents maxima to the East on the Istrian coast between Rt Zub and Savudrija, and a local maximum to the North in proximity of the coastal lagoon to the East of Bibione – P.ta Tagliamento.

Tidal ellipses fot the dominant tidal harmonics are presented in Fig. 7, with Table 3 summarizing tidal harmonic analysis results for six grid points in the radar domain. Consistently with the results of the spectral analyses, the dominant diurnal tidal harmonics (K_1,P_1) are characterized by a clockwise-rotating pattern which becomes counterclockwise only at isolated spots southwest Rt Zub. This discrepancy is anyway not significant due to the high level of uncertainties in the ellipse minor axes estimates. Both constituents increase in amplitude northwards in direction of the Italian coast and present a circular pattern towards the entrance of the Trieste Gulf, with a more elliptical pattern oriented following the coastline in proximity of the coastal lagoon to the North. Phases (and amplitudes) of the K_1 harmonic increase eastwards in direction of the Istrian coast consistently with the dynamics of a topographic wave traveling across the basin.

Table 3
Tidal ellipse parameters (major and minor axes; inclination and phase angles) with their errors for the dominant tidal constituents in the Adriatic Sea. Results are summarized for three points in the radar domain (see Fig. 1 for their location). Units are $cm\ s^{-1}$ for major and minor axes, degrees for inclinations and phases.

Constituent	Major	Error	Minor	Error	Phase	Error	Inclination	Error
[a] Grid point 166								
O1	0.41	0.59	0.09	0.51	161	80	80	110
P1	3.14	0.81	−2.06	0.68	175	33	259	35
K1	2.53	0.69	−1.63	0.61	34	34	349	37
N2	0.69	0.52	−0.3	0.65	77	98	198	81
M2	2.49	0.66	0.73	0.95	105	18	192	19
S2	1.96	0.7	0.52	0.65	38	26	132	25
K2	0.5	0.49	0.3	0.51	63	92	162	98
[b] Grid point 628								
O1	0.65	0.5	0.09	0.63	92	70	330	54
P1	2.18	0.8	−1.4	0.59	179	35	210	37
K1	2.9	0.62	−1.09	0.62	44	18	335	17
N2	1.17	0.43	−0.21	0.47	90	27	177	24
M2	4.85	0.41	0.28	0.49	89	5	172	5
S2	3.25	0.42	0.62	0.46	96	8	185	8
K2	0.91	0.32	0.16	0.35	73	28	170	25
[c] Grid point 1174								
O1	1.01	0.55	0.017	0.71	126	47	334	41
P1	1.59	0.77	0.19	0.73	16	29	325	32
K1	2.98	0.64	−0.84	0.65	45	15	331	16
N2	0.92	0.52	−0.7	0.63	75	96	165	72
M2	4.02	0.45	−1.68	0.85	95	16	164	11
S2	3.08	0.55	−0.27	0.7	129	14	163	13
K2	0.84	0.41	−0.01	0.6	99	53	190	29

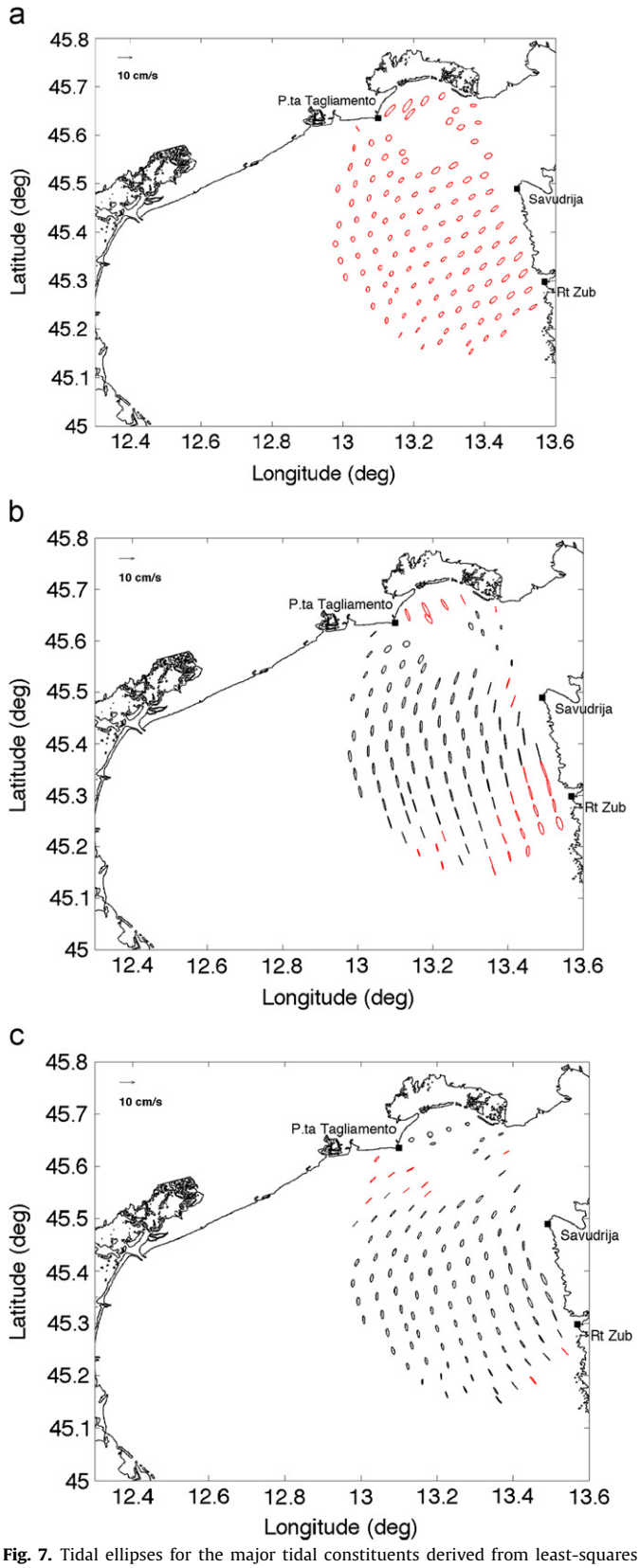

Fig. 7. Tidal ellipses for the major tidal constituents derived from least-squares tidal analysis of surface currents for the period December 2007–August 2008 when three antennas were operative. Fom top to bottom: K_1 ([a]), M_2 ([b]), S_2 ([c]). Ellipses are depicted in red if their sense of rotation is anticyclonic (clockwise). Ellipses are subsampled on a 4 km × 4 km grid for clarity.

Semidiurnal tidal constituents are characterized by a rectilinear pattern in the major part of the domain, with a dominant counterclockwise sense of rotation with the exception of a few isolated spots where they present clockwise rotation. As for the diurnal constituents, the high level of uncertainties in ellipse parameter estimates do not allow nor for an unbiased estimate of the sense of rotation in these points neither their inclinations. Ellipses tend to be aligned with the Istrian coastline in the majority of the area, and veer northeastwards toward the Trieste Gulf entrance at the corner of the peninsula. To the North, M2 ellipses increase their magnitude in proximity of the coastal lagoon along the italian coast (Fig. 7).

3.5. Empirical orthogonal function (EOF) analysis

The EOF decomposition extracts from surface current maps a limited amount of statistically significant modes of variability. The convergence rate in the eigenvalue spectrum is fast for the first three modes, which account together for 68% of total current variance. Longer convergence rate is observed for higher-order modes since more than 35 EOF modes are required to reach the 95% cumulative variance threshold.

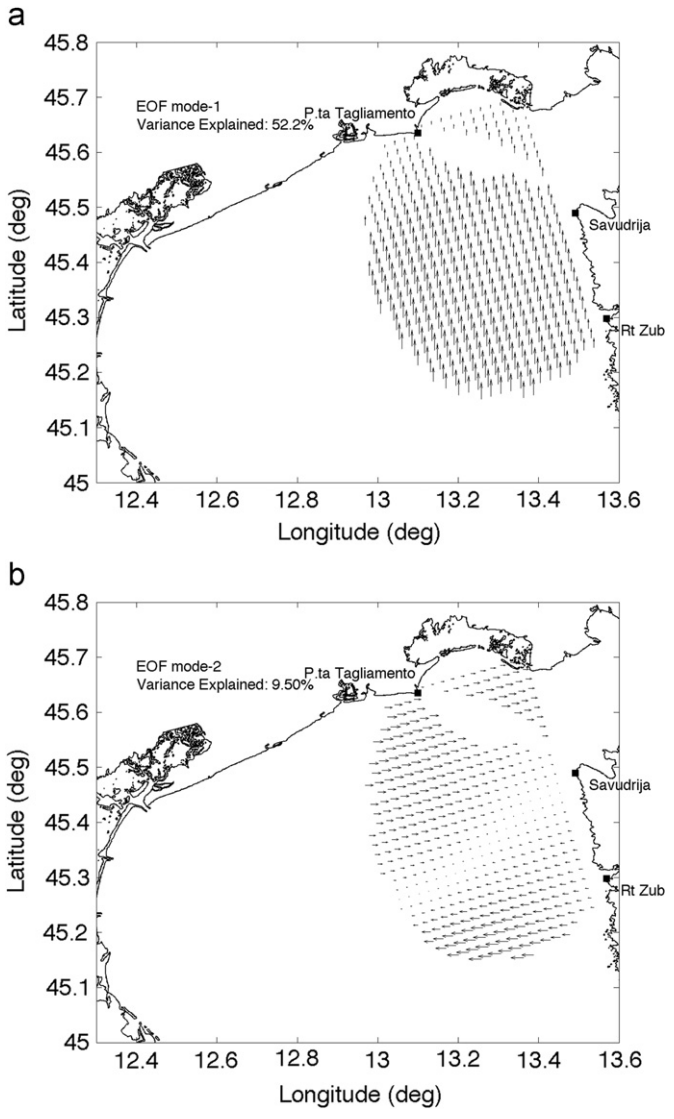

Fig. 8. The first two dominant EOF modes extacted from surface current fields for the period December 2007–August 2008 when three radars were simultaneously operative.

The first dominant EOF mode (Fig. 8a) accounts for 52% of current variance and has a spatially uniform pattern that represents the low-frequency cyclonic circulation scheme. The temporal coefficients for this mode (not shown) contain both low-frequency motions, tidal oscillations in the diurnal and semidiurnal frequency bands, and extracted a major fraction of inertial-period oscillations. The spatial patterns of EOF mode-2 (10% variance; Fig. 8b) and mode-3 (6% variance; Fig. 8c) add complexity to the basic uniform flow represented by EOF-1 since they introduce the coastal-jet feature to the North along the Italian coast (Mode-2 and Mode-3). Mode-2, in particular, adds curvature to the current field with an inflow–outflow dynamics in the Trieste Gulf area to the North, and a large cyclonic recirculation cell in the southern area. Along with the coastal-jet feature to the North, the third largest EOF mode introduces shear between the coastal strip of Istria to the East, and the open-sea area to the West connected by a eddy-like structure in the northwestern area offshore Punta Tagliamento. Higher order modes represent a combination of unresolved high-frequency motions or noise.

3.6. Wind forcing: correlation and coherence analyses

Correlation and coherence analyses show that wind forcing is important and acts over a relatively broad band of frequencies. Although being different in its northern, central and in the southern areas, the basin's response to wind forcing is immediate since there is no appreciable lag to wind within the radar domain (Table 4). Time-lagged correlation analysis between non-tidal currents and wind stress time series shows no significant delay with respect to wind forcing. The correlation peak is observed between 0-hour and 3-hour time lag, and is followed by a fast decay in correlation amplitude and an increase in veering angle up to 9-hours time lag.

Correlation between non-tidal currents (i.e., with tidal components removed) and wind stress is highest to the North (grid points 157, 166), and it weakens in a southwards direction (Table 5). In general, current vectors are directed to the right of wind stress vectors. To the north (grid points 157, 166), magnitude of vector correlation is $\rho = 0.48$–0.46, with veering angles of $\theta = 25^\circ$ and 20°. In the central area (grid points 619 and 628), correlation is $\rho = 0.37$ and both locations, with veering angles of $\theta = 35^\circ$ and 44° respectively. To the South, correlation is weakest and veering angles are zero-valued or negative (grid points 1165 and 1174), suggesting that currents in the area are not directly correlated to wind forcing. In the subtidal frequency band ($\omega > 0.03$ cph), correlation magnitudes show a significant increase in the entire area and as for the non-tidal currents, they decrease in a southwards direction. Correlation magnitude is $\rho = 0.64$–0.59 at grid points 157 and 166 (veering angles $\theta = 25^\circ$ and 21°, respectively), $\rho = 0.49$–0.47 (veering angles

Table 4
Time-lagged correlation between wind stress and surface currents at three locations in the radar coverage (see Fig. 1 for their location on the domain).

Time lag (h)	Correlation magnitude			Veering angle (deg.)		
	gp157	gp619	gp1165	gp157	gp619	gp1165
0	0.48	0.37	0.17	26.6	35.1	5.3
3	0.47	0.36	0.15	27.9	39.2	18.7
6	0.40	0.30	0.11	24.2	43.4	28.6
9	0.35	0.24	0.07	16.8	42.1	23.6
12	0.32	0.20	0.05	10.8	35.2	0.1
15	0.29	0.19	0.06	7.9	31.8	−4.5
18	0.25	0.18	0.07	5.2	34.1	16.0
21	0.21	0.15	0.05	−0.5	37.6	46.0
24	0.19	0.11	0.04	−5.3	32.5	73.1
27	0.17	0.10	0.01	−10.4	20.1	115.8

Table 5
Vector correlation between surface currents and wind stress data from the ALADIN wind model for six grid points in the radar domain (see Fig. 1 for their location). Magnitude and phase of the complex correlation are computed for surface currents with tides ([a]), on the non tidal ([b]), and on the low-frequency detided currents ([c]) time series. The veering angle correspond to the average cyclonic angle of current vectors with respect to the wind stress vector. 95% confidence levels (CL) are also provided for magnitude and veering angles.

Grid point	Magnitude	95% CL	Veering	95% CL
[a]				
157	0.47	[0.45; 0.49]	27	[25.6; 29.2]
166	0.45	[0.44; 0.47]	21	[19.4; 22.6]
619	0.37	[0.35; 0.38]	30	[27.7; 32.4]
628	0.38	[0.36; 0.40]	39	[36.8; 40.9]
1165	0.19	[0.17; 0.20]	−15	[−20.1; −9.9]
1174	0.20	[0.18; 0.20]	−3	[−6.3; 1.4]
[b]				
157	0.48	[0.46; 0.50]	25	[23.6; 26.7]
166	0.46	[0.44; 0.47]	20	[18.6; 21.8]
619	0.37	[0.35; 0.38]	35	[32.7; 37.3]
628	0.37	[0.35; 0.39]	44	[42.0; 45.9]
1165	0.15	[0.14; 0.16]	−7	[−12.6; 0.48]
1174	0.20	[0.19; 0.22]	0	[−3.6; 4.6]
[c]				
157	0.64	[0.62; 0.66]	25	[24.2; 26.5]
166	0.59	[0.57; 0.60]	21	[20.1; 22.3]
619	0.49	[0.47; 0.51]	37	[35.0; 38.5]
628	0.47	[0.44; 0.49]	47	[45.7; 48.7]
1165	0.21	[0.19; 0.22]	−7	[−12.2; −0.84]
1174	0.27	[0.25; 0.28]	2	[−1.3; 4.4]

$\theta = 37^\circ$ and 47°) in the central area, and decreases to $\rho = 0.21$–0.27 in the southern area (grid points 1165 and 1174).

Coherence spectra (Fig. 9) between non-tidal currents and wind stress for the northern and central areas show high coherence in the low-frequency band, with coherence values higher in the northern sector and lower to the South. In the northern and central portion of the radar domain, coherence is in the range $\gamma = 0.4$–0.7, and decreases on the contrary ($\gamma = 0.2$–0.4) in the southern area offshore Rt Zub. Coherence is higher in the cyclonic spectrum along the Italian coast to the North, while to the South low-frequency oscillations have larger coherence with wind stress in the anticyclonic spectrum. In the diurnal band coherence is also high and comparable in magnitude with the low-frequencies ($\gamma = 0.3$–0.7); furthermore, it is larger in the anticyclonic spectrum, and it decreases in a southwards direction as distance from the italian coast increases. No significant coherence is observed in the high-frequency band ($\omega > 0.1$ cph).

3.7. High-frequency band variability: non-tidal diurnal-period oscillations and inertial motions

Surface current spectra revealed the presence of energetic components within the diurnal and inertial frequency bands, the former being attributed to the diurnal-band tidal components (K_1 harmonic). Variance in this frequency band tend to follow the seasonal evolution of wind energy in the same frequency band (Fig. 6; Table 6). Fraction of this energy is also retained in this frequency band even after diurnal tides have been removed. This signal is also present in wind data both at the MAMBO1 buoy and the ALADIN winds (Table 6). Coherently with the seasonal cycle of the diurnal sea-breezes and the variance minimum in wind records in October 2007–March 2008 (Fig. 6), diurnal-band variance levels in surface currents is generally low ($4\ \mathrm{cm^2\ s^{-2}}$ to $8\ \mathrm{cm^2\ s^{-2}}$) during winter (December 2007 to February 2008), when they contribute to 4%–6% non-tidal variances in the majority of the radar domain. On the other hand, wind-driven diurnal-band variance levels increase northwards and reach a maximum ($45\ \mathrm{cm^2\ s^{-2}}$, corresponding to

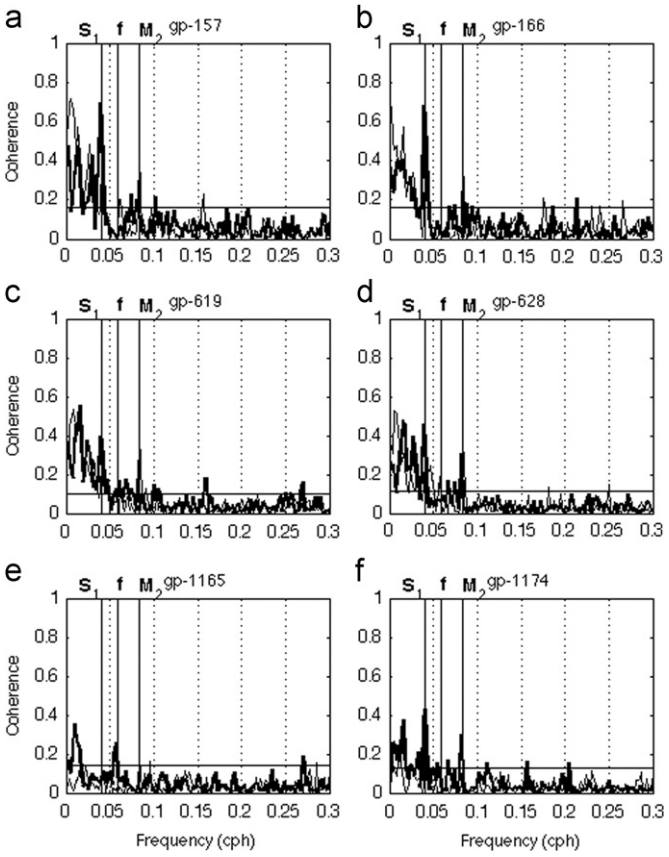

Fig. 9. Coherence between non-tidal currents and wind stress series at six grid points (grid points 157, 166, 619, 628, 1157, and 1166) shown in Fig. 1. Thin lines refer to the cyclonic motions, bold lines represent anticyclonic oscillations. The 95% confidence level for coherence is also evidenced. Vertical lines show the position of the semidiurnal, inertial and diurnal frequencies.

$6.7\ \mathrm{cm\ s^{-1}}$ rms value) in proximity of the Trieste Gulf entrance in the summer season (May – August 2008). Isolines of the distribution of non-tidal variance explained by non-tidal diurnal period variances (Fig. 10a), shows a smooth and uniform increase in a northeastward direction where the contribution is largest and more than 15% of non-tidal variance is accounted for by diurnal-period oscillations.

Inertial oscillations appear in the current spectra as wide peaks between the semidiurnal and diurnal frequencies in the anticyclonic part of the spectra. Similarly to the diurnal wind-driven currents, they show both a seasonal variability with variance maxima during summer months (Fig. 10b) along with a non homogeneous distribution within the study area. As for diurnal-period currents, inertial variances are low in winter ($5\ \mathrm{cm^2\ s^{-2}}$) and contribute weakly to non-tidal current variance (3%–4%). During summer, inertial variances increase southwestwards up to one order of magnitude than winter season, reaching their maximum amplitudes offshore Rt Zub (up to $90\ \mathrm{cm^2\ s^{-2}}$, corresponding to a $9.5\ \mathrm{cm\ s^{-1}}$ rms value) coherently with the spectral analysis results (Fig. 5). Isolines of the percent ratio inertial to non-tidal variance (Fig. 10b) show a quick increase from the northeastern corner (Trieste Gulf entrance), with inertial oscillations explaining up to 22% of non tidal variance in the central area.

3.8. Subtidal low-frequency: wind-driven patterns

In order to characterize the typical current patterns occurring under the dominant winds (bora and sirocco), the conditional-average approach was applied following Gačić et al. (2009). Wind data were divided into north-easterly bora events (winds from

Table 6
As for Table 3, but for wind time series at the "MAMBO-1" buoy in the Trieste Gulf, and for ALADIN wind time series at grid points coincident to surface current locations considered in Table 5. Units are cm s^{-1} for major and minor axes, degrees for inclinations and phases.

[a]	MAMBO buoy							
Constituent	Major	Error	Minor	Error	Inclination	Error	Phase	Error
O1	4.1	12.7	−0.1	11.2	54	110	242	175
P1	67.8	24.6	15.1	21.6	80	20	57	20
K1	58.1	22.4	−8.4	20.1	81	21	343	24
N2	11.2	9.3	1.7	12.2	30	79	228	63
M2	10.9	10.6	−2.2	9.2	90	48	82	79
S2	36.2	14.1	−1.9	10.2	82	14	3	21
K2	7.8	6.1	3.7	8.3	1	100	222	83
[b]	Grid point 166							
	Major	Error	Minor	Error	Phase	Error	Inclination	Error
O1	12.3	16.1	−5.9	16.2	3	99	29	122
P1	45.4	24.2	16.6	24.3	44	39	80	37
K1	33.4	21.3	−3.4	22.1	80	43	15	38
N2	7.2	10.5	2.5	12.2	76	119	202	115
M2	10.7	12.1	6.4	11.4	159	75	48	108
S2	43.2	13.1	−1.5	12.3	17	19	55	20
K2	6.5	8.7	−4.9	16.6	113	209	144	110
[c]	Grid point 628							
	Major	Error	Minor	Error	Phase	Error	Inclination	Error
O1	9.4	15.6	0.2	15.2	55	113	306	125
P1	71.2	21.9	7.9	24.1	35	19	61	20
K1	61.7	20.9	−9.5	23.6	57	22	17	20
N2	10.5	10.2	−0.4	10.4	52	73	252	69
M2	7.3	9.7	5.6	10.3	39	114	265	144
S2	47.2	13.2	2.5	10.1	22	14	43	16
K2	9.8	7.8	−1.5	8.4	102	74	236	57
[d]	Grid point 1174							
	Major	Error	Minor	Error	Phase	Error	Inclination	Error
O1	9.5	15.4	1.5	14.1	73	97	290	125
P1	46.9	20.6	13.1	21.2	15	31	30	30
K1	30.2	19.5	−7.5	18.2	22	47	346	43
N2	6.2	9.9	3.06	10.2	31	104	142	130
M2	5.0	8.9	−21.2	10.1	125	115	19	147
S2	39.8	13.8	−15.5	11.5	178	21	211	27
K2	7.1	8.1	0.6	9.3	155	80	192	96

the first quadrant), and southeasterly sirocco events (winds from the second quadrant), and the average current fields under these conditions extracted. Results are presented in Fig. 11a for bora wind conditions, and in Fig. 11b for sirocco winds. The resulting patterns are somewhat different in terms of current velocities and as for the resulting circulation features. Under easterly bora winds, there is a significant intensification in the coastal-jet to the north and a cyclonic cell appearing in the southernmost area. Maximum current velocities occurring during these events may reach 1 m s^{-1} maximum amplitude, especially when winds exceed 20 m s^{-1}. The current pattern that develops during southerly sirocco winds is smoother and more homogeneous than that occurring with bora. In the sirocco wind regime, the conditionally-averaged amplitudes are typically 10 cm s^{-1} directed northwards in the majority of the radar coverage. Only in the northern part they decrease and tend to curve southwestwards following the italian coast to form a small-scale cyclonic eddy to the southwest of BBIN – P.ta Tagliamento radar.

4. Discussion and conclusions

This paper describes the circulation patterns in the northerneastern Adriatic Sea using surface current measurements collected with high-frequency radar observations, and wind model data, for the period September 2007–August 2008. Results show that surface currents are primarily driven by winds and only to a smaller extent by tides. Wind forcing determines a wide variety of processes occurring at different temporal and spatial scales, and covers a broad spectrum of frequencies. Current fields evolve in space and time according to three dominant modes of variability that describe the low-frequencies, the tidal forcing and the majority of high-frequency non tidal oscillations (EOF mode-1), and add divergence and vorticity to current fields (EOF mode-2 and mode-3).

The time-averaged flow field present the expected cyclonic pattern, consistent with the EAC/WAC system derived from both observations and numerical simulations of the Adriatic Sea circulation (Artegiani et al., 1997a, 1997b; Orlić et al., 1992; Poulain, 1999; Poulain et al., 2001; Ursella et al., 2006; Kuzmić et al., 2006; Martin et al., 2007). It is persistent in time, since it repeats on a monthly time scale with only minor departures from the basic scheme. Time-averaged currents are weak in most of the domain (maximum amplitudes up to 15 cm s^{-1}) and increase northwards in the direction of the Italian coast. This is consistent with the dynamics of the vorticity-preserving flow of the EAC–WAC system (Hopkins et al., 1996).

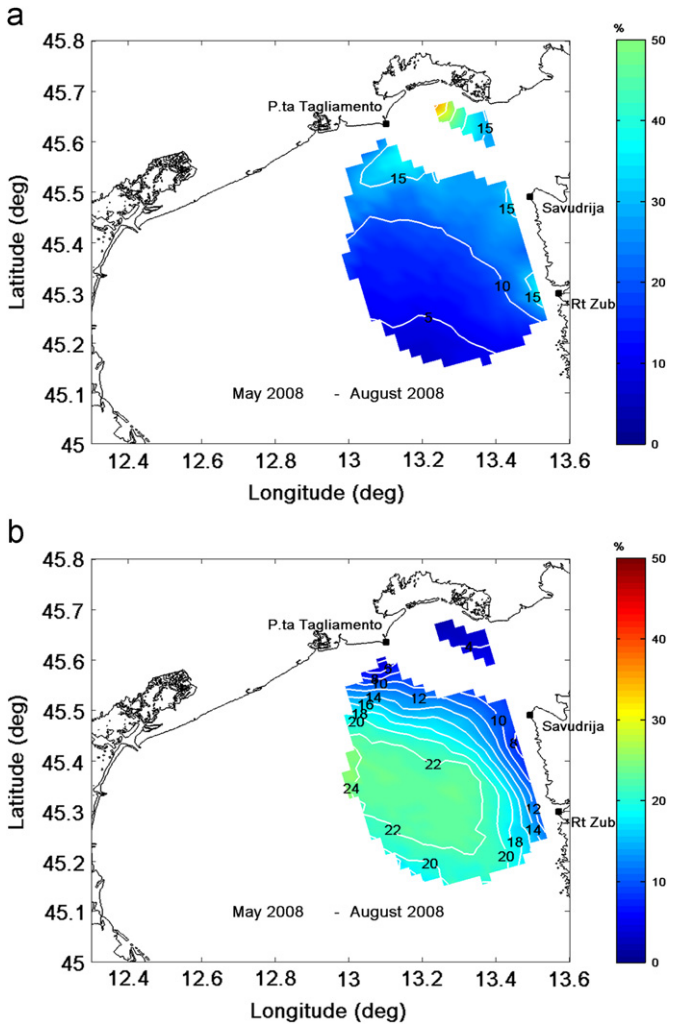

Fig. 10. Percent variance of non-tidal surface currents explained by diurnal–period ([a]) and inertial oscillations ([b]) for summer season (May 2008–August 2008).

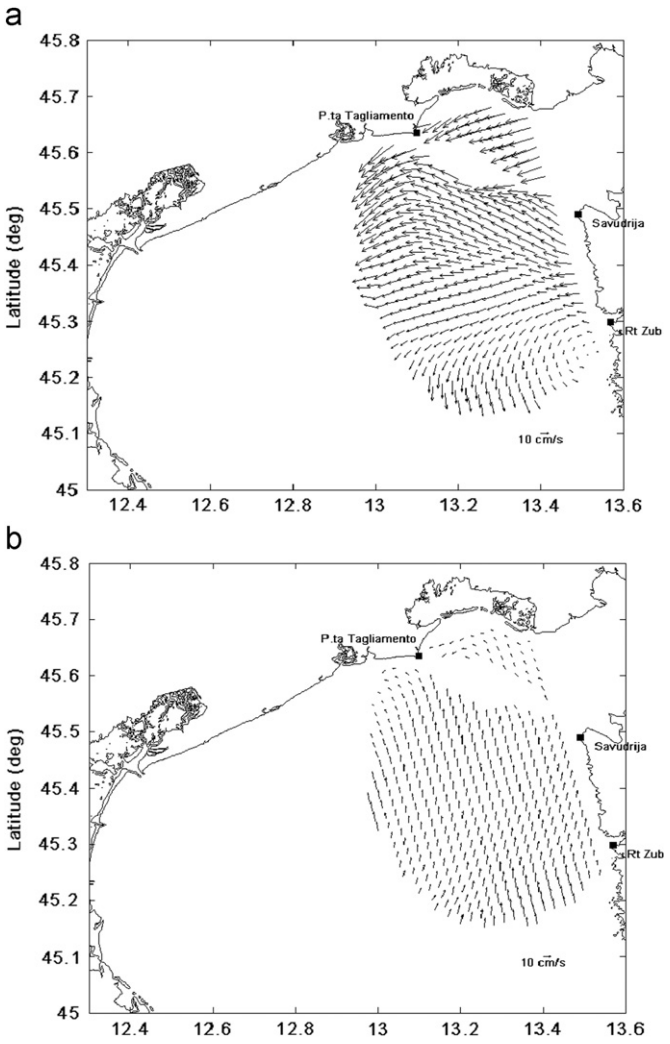

Fig. 11. Conditionally–averaged surface current pattern with bora wind forcing ([a]) and with sirocco wind forcing ([b]).

Rather than being artifacts due to poor geometrical constraints, the near zero-valued velocities in the southwestern corner and the corresponding curvature are consistent with a wider sub-basin scale cyclonic cell also described in recent numerical simulations which are currently being compared and interpreted with HF radar measurements in the area. Similarly, the deviations from the jet-like structure in the northwestern corner to the south of BBIN – P.ta Tagliamento radar can be explaind in terms of the interaction with the freshwater plume of the Tagliamento river.

Relative vorticity (ζ_{HF}) is prevalently positive depending either on flow curvature or current shear. Current vorticity shows a persistent positive maximum in the northern part of the study area, due partly to the shallower depth and the vorticity imparted to the current field by bora wind pulses, that enhance the coastal-jet and trigger a complex cyclonic and anticyclonic gyre system (Cushman-Roisin and Korotenko, 2007; Jeffries and Lee, 2007; Pullen et al., 2007; Orlić et al., 1994). Fresh water inputs and the lower depths can also be invoked to explain the localized vorticity maximum observed in this area, as suggested from the above mentioned numerical simulations.

Divergence is prevalently positive and follows changes in relative vorticity in the interior of the radar domain. In agreement with estimates derived from Eulerian statistics of satellite-tracked drifters in the area (Ursella et al., 2006), relative vorticity of the time-averaged surface current field is 1 to 2 orders of magnitude smaller than the planetary vorticity (f) at the local latitudes (Ursella et al., 2006). Furthermore, relative vorticity in the area is comparable with values offshore the Venice Lagoon, where the typical magnitude is at most 10% the planetary vorticity (Gačić et al., 2009).

Tidal forcing is weak if compared to wind-driven contribution, and limited to the semidiurnal and diurnal frequency band, the latter being biased by the seasonal cycle of diurnal sea-breezes. Least-squares tidal analyses of surface currents for the 8-months period with three radars show that tidal oscillations contribute 10% to 20% to total current variance, with the maximum contribution in the coastal areas along the Italian coast and the Istrian peninsula. Only 3 out of the 7 tidal constituents usually considered in numerical models of tides in the Adriatic Sea (Janeković and Kuzmić, 2005; Gačić et al., 2000) contribute in a significant way to tidal variance. These are the semidiurnal M_2, S_2 and the diurnal K_1 constituents. Tidal ellipses for the semidiurnal tidal constituents, explained as superposition of a pair of incident/reflected Kelvin waves with an amphidromic point in the central part of the Adriatic Sea (Gačić et al., 2000), have a predominant rectilinear pattern and are oriented following the Istrian peninsula, showing a more circular pattern towards the Italian coast. As for tidal amplitudes, ellipse inclinations, and rotary coefficients, analyses show good match with numerical models of tidal currents (Cushman-Roisin and Naimie, 2002; Gačić et al., 2000)

and experimental data sets (Martin et al., 2006). Results also agree well with tidal ellipses from multi-year observation of surface currents in the northwestern Adriatic, from observations offshore Ancona and in front of the Venice Lagoon, showing rectilinear polarization of semidiurnal tides with alternating clockwise and counterclockwise rotation (Chavanne et al., 2007; Budillon et al., 2002; Kovačević et al., 2004).

The rotation is predominantly cyclonic, becoming anticyclonic only at isolated locations in the radar area. Uncertainties in the estimates of the ellipse minor axes are high, comparable with the minor axis amplitudes, and thus it is difficult to determine whether semidiurnal tides in the study area have clockwise or counterclockwise rotation. The diurnal K_1 constituent shows major discrepancies with models and previous experimental observations, since ellipses in the entire area show a circular pattern rather than a rectilinear one (Martin et al., 2006; Janeković and Kuzmić, 2005; Cushman-Roisin and Naimie, 2002; Gačić et al., 2000). Analyses of ADCP records from isolated locations close to the study area show that tides explain 10% variance of currents at 5 m depth (Martin et al., 2006). Kovačević et al., (2004) showed that tides represent up to 20% total variance of surface currents along the Italian coast offshore the Venice Lagoon, whereas phase-locked tidal currents explained less than 2% of the total variance over the 2-year record in the region to the South of the Po River (Chavanne et al., 2007).

Wind forcing acting at different scales in time and space determines sub-inertial motions (intensification of the coastal-jet), forces diurnal-band currents in the northern area and drives inertial oscillations. Time-lagged vector correlation analysis suggests an immediate response to wind forcing in the majority of the domain, with an Ekman-like response (veering angles in the range 40°–45°) in the deeper areas offshore Savudrija and P.ta Tagliamento, and a coastal-trapped jet-like feature in the coastal area to the North. There exist hints of a correlation between wind forcing and currents, but weaker magnitudes and veering angles close to zero or negative-valued suggest that the dependence is not linear.

Despite wind conditions that favor inertial oscillations are most common during winter season when bora events are stronger and more frequent (see Cushman-Roisin et al., 2001), the most energetic inertial motions occur prevalently during the warm stratified season, when inertial currents explain up to 24% non-tidal variances. Analyses of surface current records show that the response of the basin to inertial oscillations is not uniform, since both non-tidal and inertial variances increase in offshore direction towards the center of the basin. This trend is consistent with the spatial variability of energy level within the inertial frequency described offshore the Venice Littoral (Kovačević et al., 2004). Inertial oscillations are a common feature in ocean circulation since they have been reported and described at many locations in the world's oceans. In the Adriatic Sea they have been reported offshore the Venice Lagoon's area (Kovačević et al., 2004) and their presence has also been documented at several offshore locations on the Adriatic shelf during the warm stratified season (Krajcar and Orlić, 1995). Inertial currents represent the adjustment of a stratified fluid to the bora-driven currents, that appear as manifestations of internal Sverdrup waves trapped in the basin under stratified conditions (Bergamasco and Gačić, 1996; Krajcar and Orlić, 1995).

Oscillations of 24-h period appear in surface currents during the warm stratified season, centered at the frequency of the diurnal S_1 tide. Their presence at this harmonic is clear both in buoy and model wind data, and in surface currents if the least-squares tidal analysis is performed on the 13-months period August 2007–August 2008. The seasonal variability of this spectral feature, along with its non-homogeneous distribution in the area, the coherence with the wind stress in the diurnal frequency band and the results of the harmonic analyses of wind data at selected locations (Tables 3 and 4), show that a large fraction of the current variance within this frequency band is attributed to diurnal sea-breezes. Effects of this forcing, interpreted as rapidly varying diurnal sea breezes, was already described for the area offshore the Venice Lagoon (Cosoli et al., 2005). Its contamination with the diurnal astronomical tide in the same area was also documented (Cosoli et al., 2008). Diurnal wind-driven currents constitute a common feature in surface current measurements, having been documented for instance offshore Bodega (Kaplan et al., 2005), on the Texas-Louisiana continental shelf (DiMarco et al., 2000), and in the Monterey Bay area (Paduan and Rosenfeld, 1996). Similarly to inertial oscillations, diurnal currents are predominant in summer since they require vertical stratification, maximum insolation and weak low-frequency meteorological forcing (DiMarco et al., 2000). As evidenced for inertial oscillations, but opposite to them, diurnal variability has a different pattern across the basin with increasing contribution along the Italian coast and the Trieste Gulf entrance where they explain up to 15% of non-tidal variance.

The two typical wind regimes in the area (sirocco and bora winds) drive two distinct flow patterns. The relatively smooth sirocco wind drives a rather uniform northeasterly flow pattern with decreasing amplitudes in direction of the northern coast due to the pressure gradient driven by the piling up of the water on the coast. This sea-level rise drives an intense southwards return flow when wind forcing relaxes. Then, the return to the cyclonic circulation is immediate. On the other hand, the sheared structure of the bora wind forcing determines a more complex flow pattern, with the intensification of the coastal-jet on the Italian coast to the North, and the occurrence of an unreported cyclonic recirculation cell offshore Rt Zub which inverts the EAC circulation and eventually forms a closed structure. Similar structures have been extracted with a self-organizing map approach in the area (Mihanović et al., submitted for publication). Typically, the response of the Northern Adriatic Sea to bora wind-driven forcing is described as an alternating cyclonic/anticyclonic gyre system formed due to the vorticity imparted to the sea by the wind-field allowing for entrainment of the Po River plume into the double gyre system (Pullen et al., 2003; Paklar et al., 2001; Orlić et al., 1994). The majority of model simulations of bora-driven circulation (for instance, Pullen et al., 2007) did not reproduce the observed cyclonic recirculation cell, presumably due to the low-resolution wind fields used in the simulations. Numerical simulation with higher-resolution wind data and wind fields (Cushman-Roisin and Korotenko, 2007), resolved a southwards current along the southwestern shore of Istria, which was explained from a baroclinic geostrophic adjustment of the Istian coastal waters after a strong and rapid wind impulse. Experimental data collected within the NASCUM project, along with preliminary assessment of the local dynamics from high-resolution ALADIN wind fields, suggest that this unreported recirculation cell is related to the meridional gradient of wind stress curl in the area. Finally, the ICCC (Istrian Coastal Counter-Current; Supić et al., 2000) system that represents an episodic inversion of the dominant northwestwards flow in the area, was not detected during the measurement period.

References

Artegiani, A., Bregant, D., Paschini, E., Pinardi, N., Raicich, F., Russo, A., 1997a. The Adriatic Sea general circulation. Part I: air–sea interactions and water mass structure. Journal of Physical Oceanography 27, 1492–1514, 1997.

Artegiani, A., Bregant, D., Paschini, E., Pinardi, N., Raicich, F., Russo, A., 1997b. The Adriatic Sea general circulation. Part II: Baroclinic circulation structure. Journal of Physical Oceanography 27, 1515–1532, 1997.

Atwater D., Heron M., 2010. Temporal error analysis for compact cross-loop direction-finding HF radar, IEEE Oceans 2010 conference paper, 10.1109/OCEANS.2010.5664291.

Barth, A., Alvera-Azcárate, A., Gurgel, K.W., Staneva, J., Port, A., Beckers, J.M., Stanev, E., 2010. Ensemble perturbation smoother for optimizing tidal boundary conditions b assimilation of High-Frequency radar surface currents – application to the German Bight. Ocean Science 6, 161–178, 2010.

Bergamasco, A., Gačić, M., 1996. Baroclinic response of the Adriatic Sea to an episode of bora wind. Journal of Physical Oceanography 26, 1354–1369, 1996.

Book, J.W., Perkins, H.T., Cavaleri, L., Doyle, J.D., Pullen, J.D., 2005. ADCP observations of the western Adriatic slope current during winter 2001. Progress in Oceanography 66, 270–286.

Book, J.W., Signell, R.P., Perkins, H., 2007. Measurements of storm and nonstorm circulation in the northern Adriatic: October 2002 Through April 2003. Journal of Geophysical Research 112, C11S92. doi:10.1029/2006JC003556.

Breaker, L.C., Gemmill, W.H., Crosby, D.S., 1994. The application of a technique for vector correlation to problems in meteorology and oceanography. Journal of Applied Meteorology 33 (11), 1354–1365.

Budillon, G., Grilli, F., Ortona, A., Russo, A., Tramontin, M., 2002. An assessment of surface dynamics observed offshore Ancona with HF radar. Marine Ecology 23 (Supplement 1), 21–37.

Chapman, R.D., Graber, H.C., 1997. Validation of HF radar measurements. Oceanography 10 (2), 76–79.

Chavanne, C., Janeković, I., Flament, P., Poulain, P.M., Kuzmić, M., Gurgel, K.W., 2007. Tidal currents in the northwestern Adriatic: high-frequency radio observations and numerical model predictions. Journal of Geophysical Research 112, C03S21. doi:10.1029/2006JC003523.

Cosoli, S., Gačić, M., Mazzoldi, A., 2005. Comparison between HF radar current data and moored ADCP current meter. Il Nuovo Cimento 28C. doi:10.1393/ncc/i2005-10032-6.

Cosoli, S., Gačić, M., Mazzoldi, A., 2008. Variability of currents in front of the venice Lagoon, Northern Adriatic Sea. Annales Geophysicae 26, 1–16, 2008.

Cosoli S., Bolzon G., 2009. Near-real time signal-to-noise ratio quality control procedure for SeaSonde HF radars, 9th International Radiowave Oceanography Workshop, May 2009.

Cosoli, S., Mazzoldi, A., Gačić, M., 2010. Validation of surface current measurements in the Northern Adriatic Sea from High-Frequency radars. J ournal of Atmosphere and Oceanic Technology 27, 909–919.

Cushman-Roisin, B., Korotenko, K.A., 2007. Mesoscale-resolving simulations of summer and winter bora events in the Adriatic Sea. Journal of Geophysical Research 112, C11S91. doi:10.1029/2006JC003516.

Cushman-Roisin, B., Gačić, M., Poulain, P.M., Artegiani, A. (Eds.), 2001. Kluver Academic Publishers, Dordrecht, Boston London.

Cushman-Roisin, B., Naimie, C.E., 2002. A 3D finite element model of the Adriatic Sea tides. Journal of Marine System 37, 279–297.

DiMarco, S.F., Howard, M.K., Reid, R.O., 2000. Seasonal variation of wind-driven diurnal current cycling on the Texas–Luisiana continental shelf. Geophysical Research Lett 27 (7), 1017–1020.

Emery, W.J., Thomson, R.E., 2004. Data Analysis Methods in Physical Oceanography. Elsevier B.V. second and revisededition, 2004.

Emery, B.M., Washburn, L., Harlan, J.A., 2004. Evaluating radial current measurements from Codar High-Frequency radars with moored current meter. Journal of Atmospheric Oceanic Technology 21, 1259–1271.

Efron, B., Tibshirani, R., 1986. Bootstrap methods for standard errors, confidence intervals, and other measures of statistical accuracy. Statistical Sciences 1 (1), 54–77.

Gačić, M., Kovačević, V., Cosoli, S., Mazzoldi, A., Paduan, J.D., Mosquera, I.Mancero, Yari, S., 2009. Surface current patterns in front of the Venice Lagoon. Estuarine Coast. Shelf Science 82, 485–494.

Gonella, J., 1972. A rotary-component method for analyzing meteorological and oceanographic vector time series. Deep-Sea Res 19, 833–846.

Gurgel K.W., 1994. Shipborne measurements of surface current fields by HF radar. *L'Onde Electrique – September-Octobre 1994*, Vol. 74, N.5.

Hopkins T.S., Artegiani A., Bignami F., Russo A., 1996. Water mass modification in the Northern Adriatic. A preliminary assessment from the ELNA hydrography, in The Adriatic Sea, edited by T. S. Hopkins et al., Ecosyst. Res. Rep. 32, pp. 85–106, Eur. Comm., Brussels.

Janeković, I., Kuzmić, M., 2005. Numerical simulation of the Adriatic Sea principal tidal constituents. Annales Geophysicae 23, 3207–3218 SRef-ID: 1432-0576/ag/2005-23-3207.

Jeffries, M.A., Lee, C.M., 2007. A climatology of the northern Adriatic Sea's response to bora and river forcing. Journal of Geophysical Research 112, C03S02. doi:10.1029/2006JC003664.

Ivatek-Šahdan, S., Tudor, M., 2004. Use of high-resolution dynamical adaptation in operational suite and research impact studies. Meteorologische Zeitschrift 13 (2), 99–108.

Kaihatu, J.M., Handler, R.A., Marmorino, G.O., Shay, L.K., 1998. Empirical orthogonal function analysis of ocean surface currents using complex and real-vector methods. Journal of Atmosphere Oceanic Technology 15, 927–941.

Kaplan, D.M., Largier, J., Botsford, L., 2005. HF radar observations of surface circulation off Bodega Bay (northern California, USA). Journal of Geophysical Research 110, C10020. doi:10.1029/2005JC002959.

Kundu, P.K., 1976. Ekman veering observed near the ocean bottom. Journal of Physical. Oceanography 6, 238–241.

Large, W.G., Pond, S., 1981. Open ocean momentum flux measurements in moderate to strong winds. Journal of Physical. Oceanography 11, 324–336, 1981.

Kohut, J.T., Glenn, S.M., 2003. Improving HF radar surface current measurements with measured antenna beam patterns. Journal of Atmosphere Oceanic Technology 20, 1303–1316.

Kovačević, V., Gačić, M., Mazzoldi, A., Dallaporta, G., Gaspari, A., 2000. Sea-surface currents measured by coastal HF radar offshore Ancona. Bollettino di Geofisica Teorica ed Applicata 41 (3–4), 339–355.

Kovačević, V., Gačić, M., Mancero-Mosquera, I., Mazzoldi, A., Marinetti, S., 2004. HF radar observations in the northern Adriatic: Surface current field in front of the Venetian Lagoon. Journal of Mar. System 51, 95–122.

Krajcar, V., Orlić, M., 1995. Seasonal variability of inertial oscillations in the Northern Adriatic. Continental Shelf Research 15, 1221–1233.

Kuzmić, M., Janeković, I., Book, J.W., Martin, P.J., Doyle, J.D., 2006. Modeling the northern Adriatic double-gyre response to intense bora wind: A revisit. Journal of Geophysical Research 111, C03S13. doi:10.1029/2005JC003377 [printed 112(C3), 2007].

Gačić, V., Viezzoli, D., Cushman-Roisin, B., 2000. Tidal dynamics in the northern Adriatic Sea. Journal of Geophysical Research 105 (C11), 26,265–26,280.

Marmorino, G.O., Shay, L.K., Haus, B.K., Handler, R.A., Graber, H.C., Horne, M.P., 1999. An EOF analysis of HF Doppler radar current measurements of the Chesapeake Bay buoyant outflow. Continental Shelf Research 19, 271–288.

Martin, P.J., Book, J.W., Doyle, J.D., 2006. Simulation of the northern Adriatic circulation during winter 2003. Journal of Geophysical Research 111, C03S12. doi:10.1029/2006JC003511 [printed 112(C3), 2007].

Mazzoldi A., Bortoletto M., Dallaporta G., Gaspari A., 1998. Coastal Oceanography: Surface current measurements by HF radars. The SeaSonde system. CNR-ISMAR, Technical Report 224, 27 pages.

Mihanović H., Cosoli S., Vilibić I., Ivanković D., Dadić V., Gačić M., 2011. Surface current patterns in the northern Adriatic extracted from HF radar data using Self-Organizing Map analysis. Journal of Geophysical Research 116, C08033. doi:10.1029/2011JC007104.

Orlić, M., Gačić, M., La Violette, P.E., 1992. The currents and circulation of the Adriatic Sea. Oceanologia Acta 15, 109–124.

Orlić, M., Kuzmić, M., Pasarić, Z., 1994. Response of the Adriatic Sea to the bora and sirocco forcing. Continental Shelf Research 14, 91–116.

Paduan, J.D., Graber, H.C., 1997. Introduction to high frequency radar: reality and myth. Oceanography 10 (2), 36–39.

Paduan, J.D., Rosenfeld, L.K., 1996. Remotely sensed surface currents in Monterey Bay from shore-based HF radar (CODAR). Journal of Geophysical Research 101, 20669–20686.

Pawlovitz, R., Beardsley, B., Lentz, S., 2002. Classical tidal harmonic analysis including error estimates in MATLAB using T_TIDE. Comput. Geosci. 28, 929–937.

Paklar, G.B., Isakov, V., Koračin, D., Kourafalou, V., Orlić, M., 2001. A case study of bora-driven flow and density changes on the Adriatic Shelf (January 1987). Continental Shelf Research 21, 1751–1783.

Poulain, P.-M., 1999. Drifter observations of surface circulation in the Adriatic Sea between December 1994 and March 1996. Journal of Marine System 20, 231–253.

Poulain, P.-M., 2001. Adriatic Sea surface circulation as derived from drifter data between 1990 and 1999. Journal of Marine System 29, 3–32.

Pullen, J., Doyle, J.D., Hodur, R., Ogston, A., Book, J.W., Perkins, H., Signell, R., 2003. Coupled ocean-atmosphere nested modelling of the Adriatic Sea during winter and spring 2001. Journal of Geophysical Research 108 (C10), 3320. doi:10.1029/2003JC001780.

Pullen, J., Doyle, J.D., Haack, T., Dorman, C., Signell, R.P., Lee, C.M., 2007. Bora event variability and the role of air-sea feedback. Journal of Geophysical Research 112, C03S18. doi:10.1029/2006JC003726.

Sanderson, B.G., 1995. Structure of an eddy measured with drifters. J. Geophysical Research 100 (C4), 6761–6776.

Supić, N., Orlić, M., Degobbis, D., 2000. Istrian Coastal Countercurrent and its year-to-year variability. Estuarine Coastal Shelf Sci 51, 385–397.

Supić, N., Orlić, M., Degobbis, D., Dakovac, T., Krajcar, V., Precali, R., 2000b. Occurrence of the Istrian Coastal Countercurrent in 2000, a year with a mucilage event. Geofizica 18–19 (2001–2002), 45–57.

Supić, N., Orlić, M., Degobbis, D., 2003. Istrian Coastal Countercurrent in the year 1997. Il Nuovo Cimento 26C, 2.

Ursella, L., Poulain, P.M., Signell, R.P., 2006. Surface drifter derived circulation in the northern and middle Adriatic Sea: Response to wind regime and season. Journal of Geophysical Research 111, C03S04. doi:10.1029/2005JC003177 [printed 112(C3), 2007].